Chiral Seeded Growth of Gold Nanorods Into Fourfold Twisted Nanoparticles with Plasmonic Optical Activity

Bing Ni, Mikhail Mychinko, Sergio Gómez-Graña, Jordi Morales-Vidal, Manuel Obelleiro-Liz, Wouter Heyvaert, David Vila-Liarte, Xiaolu Zhuo, Wiebke Albrecht, Guangchao Zheng, Guillermo González-Rubio, José M. Taboada, Fernando Obelleiro, Núria López, Jorge Pérez-Juste, Isabel Pastoriza-Santos, Helmut Cölfen, Sara Bals,* and Luis M. Liz-Marzán**

A robust and reproducible methodology to prepare stable inorganic nanoparticles with chiral morphology may hold the key to the practical utilization of these materials. An optimized chiral growth method to prepare fourfold twisted gold nanorods is described herein, where the amino acid cysteine is used as a dissymmetry inducer. Four tilted ridges are found to develop on the surface of single-crystal nanorods upon repeated reduction of $HAuCl_4$, in the presence of cysteine as the chiral inducer and ascorbic acid as a reducing agent. From detailed electron microscopy analysis of the crystallographic structures, it is proposed that the dissymmetry results from the development of chiral facets in the form of protrusions (tilted ridges) on the initial nanorods, eventually leading to a twisted shape. The role of cysteine is attributed to assisting enantioselective facet evolution, which is supported by density functional theory simulations of the surface energies, modified upon adsorption of the chiral molecule. The development of *R*-type and *S*-type chiral structures (small facets, terraces, or kinks) would thus be non-equal, removing the mirror symmetry of the Au NR and in turn resulting in a markedly chiral morphology with high plasmonic optical activity.

1. Introduction

Chirality, which spans over both biological and abiotic systems, is one of the most fascinating geometrical properties. Chiral molecules have unique effects in many biological systems, i.e., even though their chemical composition is the same, one enantiomer may be beneficial to human health whereas the other is detrimental.[1] Therefore, controlling enantioselectivity is not just an intellectual challenge but also of great practical importance. Compared to their organic counterparts,[2,3] chirality in inorganic systems, be it individual particles or self-assembled structures, may arise either because of the nature of the crystal space group or from the morphology of the system, lacking mirror and inversion symmetry. The physics of light–matter interactions in inorganic chiral

B. Ni, G. González-Rubio, H. Cölfen
Physical Chemistry
University of Konstanz
Universitätsstrasse 10, 78457 Konstanz, Germany
E-mail: bing.ni@uni-konstanz.de

M. Mychinko, W. Heyvaert, W. Albrecht,[+] S. Bals
EMAT
University of Antwerp
2020 Antwerp, Belgium
E-mail: sara.bals@uantwerpen.be

The ORCID identification number(s) for the author(s) of this article can be found under https://doi.org/10.1002/adma.202208299.

[+]Present address: Department of Sustainable Energy Materials, AMOLF, Science Park 104, 1098 XG, Amsterdam, The Netherlands

[++]Present address: School of Science Engineering, The Chinese University of Hong Kong (Shenzhen), Shenzhen, 518172, P. R. China

DOI: 10.1002/adma.202208299

M. Mychinko, W. Heyvaert, W. Albrecht, S. Bals
NANOlab Center of Excellence
University of Antwerp
2020 Antwerp, Belgium

S. Gómez-Graña, J. Pérez-Juste, I. Pastoriza-Santos, L. M. Liz-Marzán
CINBIO
Universidade de Vigo
Departamento de Química Física
Campus Universitario As Lagoas
36310 Marcosende Vigo, Spain

J. Morales-Vidal, N. López
Institute of Chemical Research of Catalonia (ICIQ)
The Barcelona Institute of Science and Technology (BIST)
Avinguda Països Catalans 16, 43007 Tarragona, Spain

J. Morales-Vidal
Universitat Rovira i Virgili
Avinguda Catalunya, 35, 43002 Tarragona, Spain

M. Obelleiro-Liz
EM3WORKS
Spin-off of the University of Vigo and the University of Extremadura
PTL Valladares, 36315 Vigo, Spain

materials is also distinct, leading to theoretically higher optical activity (circular birefringence and circular dichroism) compared to organic materials.[4] Moreover, the optical activity can be tuned by coupling with other physical stimuli, such as magnetic fields.[5] Geometrical chirality can also impart selectivity to other processes, such as the chirality-induced spin selectivity effect.[6,7] The handedness of chiral inorganic nanoparticles (NPs) has recently been found to selectively activate biological processes,[8] thereby supporting the idea that chirality in inorganic and biological systems can be closely connected. It is therefore clear that plenty of opportunities remain for exploring the potential of inorganic chirality.

In contrast to organic asymmetric synthesis, for which various toolboxes have been developed and understood,[9,10] synthetic methodologies for chiral inorganic NPs are still limited. A reliable synthesis methodology is essential before further research can be carried out, based on these systems. Several strategies have been reported for the preparation of chiral inorganic materials, such as templated growth,[11] glancing angle deposition,[12] chiral imprinting,[13] etc.[14] Wet chemical methods have also been employed,[15–17] which yield large amounts of uniform chiral NPs in a short time, while offering a great potential to control and tune NP size and shape. Among various inorganic nanomaterials, Au NPs have attracted a great deal of attention due to their special properties, such as tunable plasmon resonances, biocompatibility, etc.[18,19] Such properties and derived applications are largely related to the possibility of tailoring the morphology of Au NPs, including chiral shapes that can lead to unprecedented applications. For example, chiral Au NPs have been used for detecting amyloid fibers in Parkinson's and prion diseases,[20] or inhibiting Aβ fibrillation related to Alzheimer's disease.[21] The synthesis of chiral Au NPs typically relies on introducing chiral additives during growth.[22] Nam and co-workers reported the use of chiral amino acids to guide the dissymmetric growth of cubic Au NPs (with a $\frac{4}{m}\bar{3}\frac{2}{m}$ symmetry, see **Figure 1**a), so that carefully optimized growth conditions led to the gradual formation of structures with helical features.[15,23] Such dissymmetric products generally feature helical shapes with rounded surfaces, which expose a variety of facets. The final nanostructures showed a 432 symmetry, which can be understood because of the elimination of the mirror symmetry in the original $\frac{4}{m}\bar{3}\frac{2}{m}$ space group (Figure 1a). A different strategy to prepare chiral Au NPs involves the use of quasi-helical micelles to guide atom diffusion during seeded growth on Au nanorods (NRs), through which intricate chiral wrinkles are developed.[16]

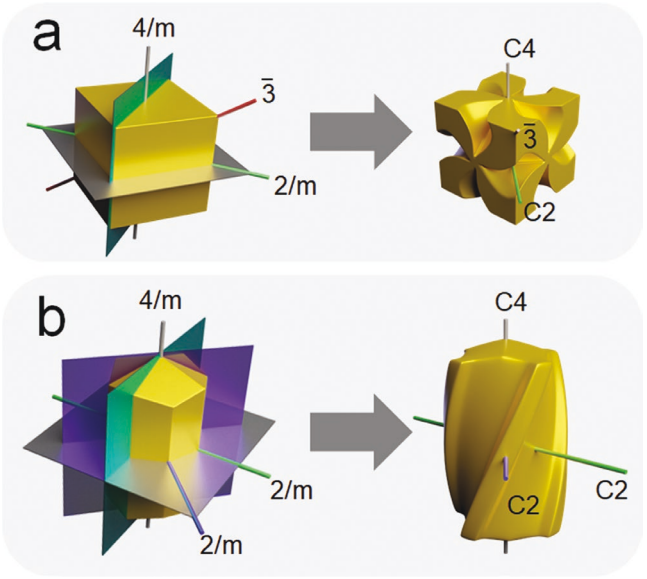

Figure 1. Symmetry analysis of different NP morphologies, where the main symmetry elements (rotation axes and mirror planes) are labeled. a) According to the Hermann–Mauguin notation, a cubic shape has a symmetry of $\frac{4}{m}\bar{3}\frac{2}{m}$. When all mirror planes are removed, a 432 symmetry is obtained. b) The single-crystal Au NR in this image (with octagonal cross-section) has a symmetry of $\frac{4}{m}\frac{2}{m}\frac{2}{m}$, written as 4/mmm in short. The rod axis is along the <001> direction, and therefore only C4 symmetry can be found in the primary direction. When all mirror planes are removed from the 4/mmm symmetry, a 422 symmetry may be obtained, as in the twisted rod.

Inspired by these works, we aimed at investigating the potential use of cysteine (cys) as a chiral ligand to direct dissymmetric growth on pre-formed Au nanorods (NRs). As described in refs. [24,25] a single-crystalline Au NR ideally has a

D. Vila-Liarte, X. Zhuo,[++] L. M. Liz-Marzán
CIC biomaGUNE
Basque Research and Technology Alliance (BRTA)
20014 Donostia-San Sebastián, Spain
E-mail: llizmarzan@cicbiomagune.es

D. Vila-Liarte, L. M. Liz-Marzán
Biomedical Research Networking Center in Bioengineering, Biomaterials, and Nanomedicine (CIBER- BBN)
20014 Donostia-San Sebastián, Spain

D. Vila-Liarte
Department of Applied Chemistry
University of the Basque Country
20018 Donostia-San Sebastián, Spain

G. Zheng
School of Physics and Microelectronics
Key laboratory of Material Physics
Ministry of Education
Zhengzhou University
Zhengzhou 450001, P. R. China

J. M. Taboada
Departamento de Tecnología de los Computadores y Comunicaciones
Universidad de Extremadura
10003 Cáceres, Spain

F. Obelleiro
Departamento de Teoría de la Señal y Comunicaciones
University of Vigo
36310 Vigo, Spain

L. M. Liz-Marzán
Ikerbasque
Basque Foundation for Science
20014 Bilbao, Spain

4/mmm symmetry. A similar transformation as that described in Figure 1a for nanocubes, can be expected to lead to twisted rodlike structures, which should have different structural features (Figure 1b). By controlling the growth parameters, we indeed obtained NRs with a twisted morphology and high chiral optical activity. Although twisted Au NRs can be readily obtained through a single seeded-growth step, both morphological and optical chirality were significantly enhanced by implementing a multistep protocol involving repeated additions of the metal precursor in small aliquots. The morphology could be additionally tuned through variations in cys concentration, growth temperature, as well as through the size and aspect ratio of the Au NR seeds. Upon characterization of the morphologies and consideration of the crystalline structures, we propose a growth model based on the enantioselective development of chiral surfaces from the initial Au NRs. Cys enhances enantioselective surface facet evolution, as supported by density functional theory (DFT) simulations, which show that the surface energies of the enantiomeric facets are different in the presence of adsorbed chiral molecules.

2. Results and Discussion

2.1. Multistep Growth of Fourfold Twisted Nanorods

The selected growth conditions in this study were similar to those typically used in the standard seed-mediated growth of Au NRs, using ascorbic acid (AA) as the reducing agent and $HAuCl_4$ as the metal precursor, but using cetyltrimethylammonium chloride (CTAC) instead of its bromide counterpart, CTAB, as previously used in the chiral growth with amino acids[15] (see details in the Supporting Information). The Au NRs used as seeds were prepared by a three-step synthesis process by which NR size and aspect ratio can be readily selected.[26] We initially focused on the chiral growth of high-aspect-ratio Au NR seeds, with an average length of 98.5 ± 8.7 nm and average width of 13.8 ± 1.4 nm (Figure S1, Supporting Information). The seeds displayed localized surface plasmon resonance (LSPR) bands centered at 508 and 1098 nm, for the transverse and longitudinal LSPR modes, respectively. Either *L*-cys or *D*-cys was added as the chiral inducer. After optimizing the concentrations for each reactant (Figures S2–S4, Supporting Information), a reproducible multistep chiral growth protocol was established.

When using an *L*-cys concentration of 75×10^{-9} M during the multistep chiral growth, the transverse LSPR mode (TM) gradually redshifted from 508 to 650 nm, whereas the longitudinal LSPR mode (LM) initially blueshifted from 1098 to 810 nm and then gradually redshifted up to 915 nm (**Figure 2**a). Meanwhile, the LM/TM peak intensity ratio was observed to steadily decrease. On the other hand, the optical activity increased progressively, as monitored through circular dichroism (CD) measurements, from which the corresponding *g*-factors were calculated. As shown in Figure 2b, a peak in the *g*-factor plot is observed near the TM position, whereas a plateau develops around the LM.

The recorded optical evolution can be correlated to structural changes during chiral growth. High-angle annular dark-field scanning transmission electron microscopy (HAADF-STEM) analysis shows the formation of twisted structures upon successive $HAuCl_4$ additions (**Figure 3**; Figure S5, Supporting Information). HAADF-STEM images show an initial increase of rod width and sharpening of tip corners after the first $HAuCl_4$ additions (Figure 3b,c), whereas twisted structures became apparent after 5 $HAuCl_4$ additions (Figure 3d) and subsequent additions reinforced the twisted appearance of the obtained NPs (Figure 3e–g; Figure S6, Supporting Information). The observed shape evolution illustrates an initial increase of the Au NRs width, in agreement with a measured redshift of the TM LSPR band and blueshift of the LM LSPR band (Figure 2a; Figure S5, Supporting Information). Thereafter, the formation of small protrusions at the tips is responsible for a gradual LM redshift.[27] Apparently, similar twisted structures with opposite handedness were obtained by using *D*-cys as the chiral inducer (Figure S7, Supporting Information). It should be noted that, when using *D*-cys, opposite CD signs were obtained, as expected for a different handedness of the obtained NPs (Figure S8, Supporting Information).

2.2. Connecting Morphology to Optical Activity

Given that conventional HAADF-STEM images are 2D projections of a 3D object, electron tomography experiments were

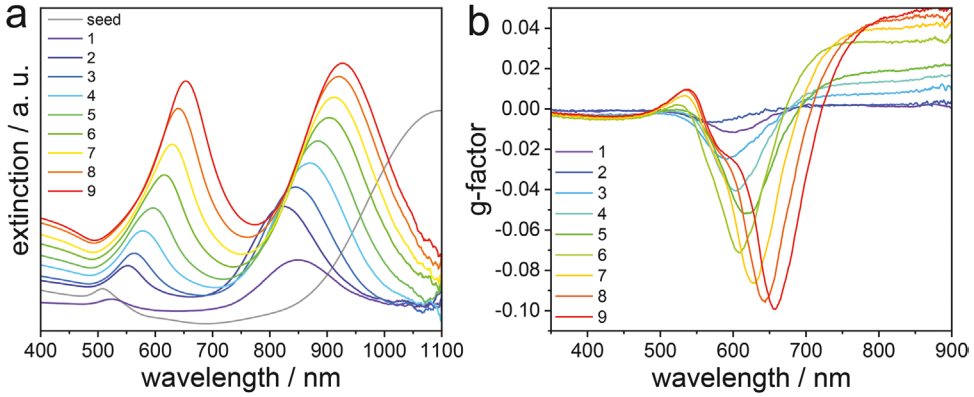

Figure 2. Evolution of Vis–NIR spectra and optical activity after successive $HAuCl_4$ additions, as labeled. (*L*-cys concentration was 75×10^{-9} M in this experiment).

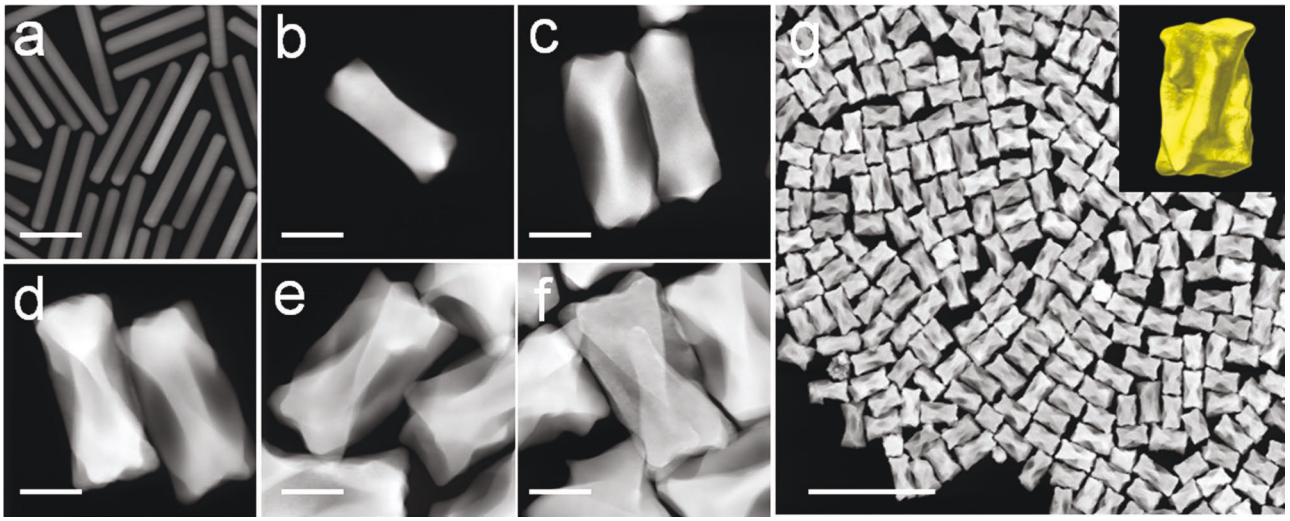

Figure 3. Evolution of twisted morphology during Au NR growth with an *L*-cys concentration of 75×10^{-9} M. a) STEM image of Au NRs used as seeds. b–f) HAADF-STEM images of the products after 1 (b), 3 (c), 5 (d), 7 (e), and 9 (f) $HAuCl_4$ additions. $[HAuCl_4]/[Au^0_{NRs}]$ increased from 2.7 (b) to 8 (c), 13.4 (d), 18.8 (e), and 24.3 (f). g) Low-magnification HAADF-STEM image of twisted Au NRs obtained after 9 $HAuCl_4$ additions. The inset shows the electron tomography reconstruction of a single chiral Au NR. Scale bars: 50 nm (a–f) and 500 nm (g).

performed for selected twisted NRs. The 3D reconstructions revealed a fourfold twisted structure along the NR length (Figure 3g inset; Movie S1, Supporting Information), in which 4 tilted ridges are obvious. If the surface roughness is not considered, this particle can be described by an ideal model that features a 422 symmetry (Figure 1b). This is not surprising because the 422 symmetry is a subset of the 4/mmm symmetry, corresponding to the seeds used for growth.[24,25] A recently reported method was employed to quantify the total helicity from electron tomography reconstructions and thereby gain insight into the chiral nature of nanoparticles (Figure S9, Supporting Information).[28] As expected, the results show mainly right-handed structures, with only one exception among 10 randomly selected NRs. The helicity of these particles is described by steep helical features, as indicated by helical inclination angles between 45 and 90°. It should be noted that no helicity was observed closer than 20 nm to the helical axis, which demonstrates that the cores are not helical. Therefore, we conclude that the observed right-handed helicity originates from the 4 tilted ridges.

Theoretical modeling based on the numerical resolution of Maxwell's equations is typically used to understand experimental measurements of plasmon resonance modes, using idealized models that resemble as close as possible the experimental morphology of interest.[29] However, the 3D objects retrieved from electron tomography reconstructions are more reliable models that can be used directly as the input morphologies for detailed electromagnetic simulations based on the boundary element method (see Supporting Information for details).[30] The simulated *g*-factor plots for several tomography reconstructions supported the hypothesis that the twisted structure is responsible for the recorded optical activity (**Figure 4**a; Figure S10, Supporting Information). Both of the simulations shown in Figure 4a further suggest that slight structural variations may lead to significant *g*-factor peak shifts, which should be taken into account because a colloidal dispersion contains a huge number of chiral NPs with minor variations in the chiral features, therefore contributing differently to the observed average optical activity.

We further simulated the near-field distributions (electric field enhancement) under illumination at 675 (Figure 4b), 650, and 900 nm (Figure S10d, Supporting Information), under left- and right-handed circularly polarized excitation. These wavelengths correspond to the simulated transversal, longitudinal LSPR modes, and the maximum of the *g*-factor magnitude, respectively. We observed that the near-field response differs significantly for both polarizations, especially at 675 nm (within the band of highest *g*-factor magnitude). The field enhancement distributions are almost complementary to each other, revealing that the origin of strong plasmonic chiroptical activity can be associated to the twisted structure along the NR length. The simulated plasmon modes under both L and R circularly polarized excitations, at different slices through the NR, can be seen in Movie S2 (Supporting Information).

2.3. Optimization of the Twisted Morphology

The experimental results show that the morphology of the final product strongly depends on cys concentration, selected from estimates of the available Au seed surface area. The highest cys concentration used in the synthesis was thus 250×10^{-9} M, which corresponds to ≈8.9% of the Au^0 NR seeds concentration, in excess of that estimated for full surface coverage (see surface coverage calculation details in the Supporting Information). When cys was excluded during the synthesis, the obtained particles showed concave sides and pointed tips but no obvious chiral features (Figure S11, Supporting Information). No optical activity was measured from these particles. With increasing cys concentration (and thus increased surface coverage), further twisting and small branches were observed to develop around the tips (**Figure 5**a,b). Such morphological changes also affected

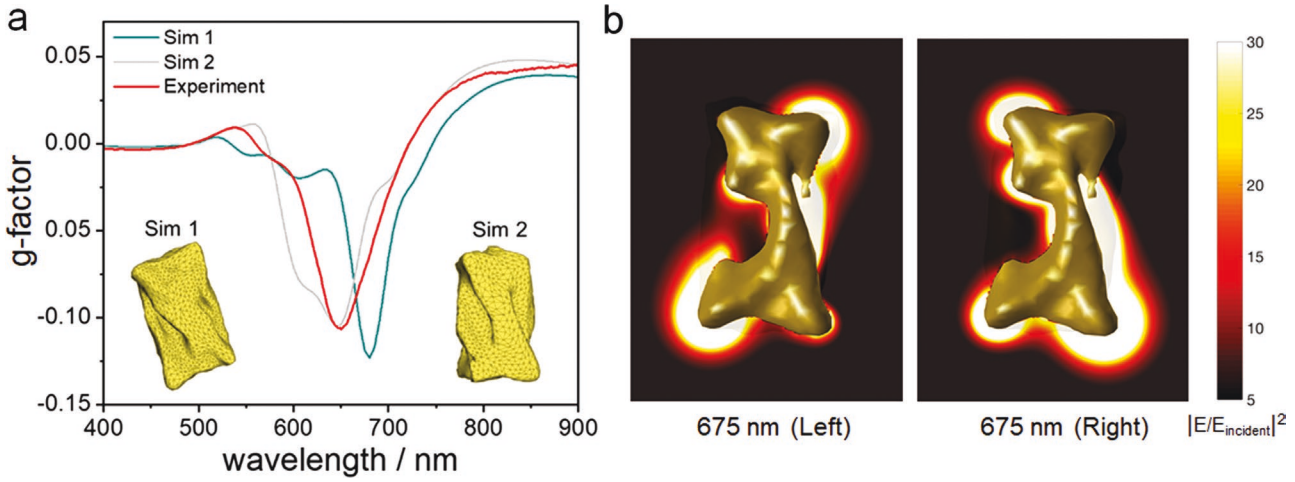

Figure 4. a) Electromagnetic simulations of the optical activity. The objects shown as insets were obtained from electron tomography reconstructions and used as the input for electromagnetic simulations (dark cyan and gray lines, as labeled). Details of the simulations can be found in Figure S10 (Supporting Information). The experimental *g*-factor spectrum (red line, corresponding to the sample shown in Figure 3g) is included for comparison. b) Simulated electric field enhancement distributions under left- and right-handed circularly polarized illumination, for the Sim 1 chiral NR in (a), calculated at 675 nm. Illumination is from behind.

significantly the resulting optical properties, leading to a gradual LSPR redshift (Figures 5c; Figure S12, Supporting Information, TM band: ≈570–720 nm; LM band: ≈850–1000 nm). When cys coverage was gradually increased, the intensities of the *g*-factor maxima were found to first increase and then decrease, with the highest values corresponding to cys concentrations in the range of ≈75–100 × 10^{-9} M and surface coverages of ≈3.6–4.8 cys nm^{-2} (Figure 5d; Figure S12, see details on coverage estimations in the Supporting Information, this value is larger than the values employed in the DFT simulations, likely due to the surface-solvent equilibrium, see below). The largest recorded *g*-factors were –0.106 (650 nm) and 0.092 (660 nm) for *L*-cys and *D*-cys as chiral inducers, respectively.

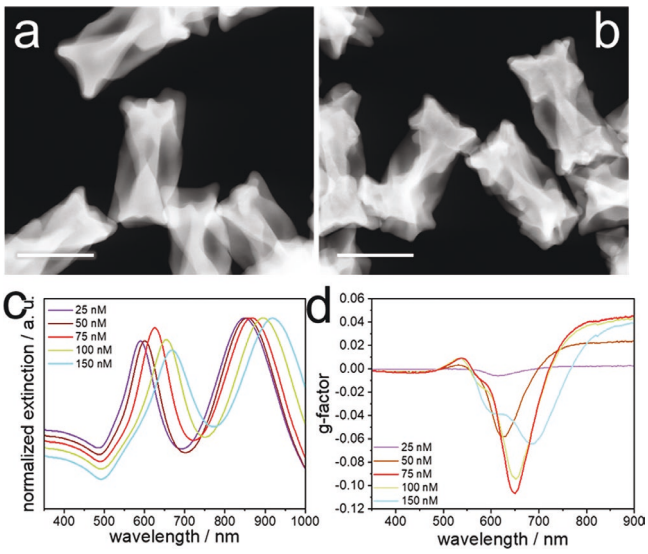

Figure 5. Influence of cys concentration (surface coverage) on the morphologies of chiral Au NRs and corresponding optical properties. a,b) STEM images for particles grown with *L*-cys concentrations of 100 × 10^{-9} M (4.8 cys nm^{-2}) (a) and 150 × 10^{-9} M (7.1 cys nm^{-2}) (b). c) Vis–NIR spectra and d) corresponding optical activity (*g*-factor) spectra for twisted Au NRs prepared with different amounts of *L*-cys, as labeled. (Additional spectra are provided in Figure S12, Supporting Information).

An additional experiment was carried out by using a racemic *D*/*L*-cys mixture as the additive in the growth solution. The resulting products also showed preferential growth at tips and caves at the sides, but only noise-level circular dichroism spectra were recorded (Figures S13 and S14; Movie S3, Supporting Information). The structural changes observed for increasing *D*/*L*-cys concentration were similar to those obtained with the individual enantiomers, i.e., higher cys concentrations resulted in more branched structures, further supporting the role of surface coverage on the growth process (Figure S13, Supporting Information). However, a 4/mmm symmetry is apparent from electron tomography analysis.

The growth temperature was used as an additional parameter to tune the resulting morphology and, in turn, the optical activity (Figure S15, Supporting Information). When seeded growth proceeded at 23 °C, the resulting twists were found to display smoother surfaces (Figure S16 and Movie S4, Supporting Information), whereas total helicity estimates (Figure S17, Supporting Information) indicated smaller values than those for the chiral rods shown in Figure 3g. Oppositely, if growth was performed at temperatures below 16 °C, relatively rough surfaces were obtained, though with poorly defined twists (results not shown). To balance these two factors and achieve a stronger optical activity, our optimized protocol involved reaction at 23 °C for the five initial $HAuCl_4$ addition steps, followed by four $HAuCl_4$ additional steps at 16 °C (Figure 3g). The rationale for this strategy was based on a lower temperature typically slowing down the reduction and diffusion of reduced atoms on the surface of the growing particles.[31] Although the high ratio between reducing agent (AA) and $HAuCl_4$ in our synthesis (≈1600) results in fast $HAuCl_4$ reduction, the diffusion of reduced atoms is still dependent on the growth temperature.

Therefore, a rougher surface would be obtained at lower temperature while relatively smoother surfaces develop at higher temperature. We additionally found that the optical activity was favored by rougher surfaces with higher anisotropy.

This optimized, multistep chiral growth method was found to achieve higher *g*-factors, as compared to the equivalent one-step growth method, which however also leads to well-defined twisted structures (Figures S18 and S19, Supporting Information). The general application of the multistep chiral growth process was further demonstrated by using Au NRs with larger and smaller dimensions as seeds (Figures S20 and S21, Supporting Information). However, each selected seed size required optimization of the reactant concentrations. In general, the magnitude of the optical activity in the final twisted products was found to decrease when using Au NR seeds with lower aspect ratios (Figure S22, Supporting Information).

2.4. Growth Mechanism

We finally aimed at understanding the growth mechanism. Due to the relatively large particle size and twisted morphology of the obtained nanostructures, it is not straightforward to determine the local crystallographic nature of their surface facets. Therefore, we selected the structures at early stages, such as the seeds (Figure 3a) and the samples obtained after the first chiral growth step (Figure 3b), for careful electron tomography analysis. The results suggest that the initial Au NRs used as seeds are enclosed by {111}, {110}, and {100} facets at the tips, while the lateral facets are a mixture of different facets resulting in rounded rods (Figure S23 and Movie S5, Supporting Information). After the first growth step, the exposed facets changed drastically (**Figure 6**; Figure S24 and Movie S6, Supporting Information). By analyzing orthoslices through the 3D reconstruction of the structure obtained after one growth step, we conclude that the lateral facets correspond to {110} planes, in agreement with the fourfold symmetry of the final products. Moreover, there are 8 (520) facets at each tip (4 bigger facets closer to the lateral sides, 4 smaller facets at the very tip). The 4 protrusions at each tip coincide with the [111] direction and are limited by the aforementioned {520}-like facets. After subsequent growth steps, these structures would evolve into fourfold twisted structures.

We therefore used this shape as the intermediated structure to understand how the mirror planes of the particle can be removed. Similar to the Au NR seed, as discussed above and presented in Figure 1b, the intermediate structure showed a symmetry close to 4/mmm, whereas the idealized twisted NR has a symmetry of 422. The transition from 4/mmm to 422, implying the removal of mirror symmetry, can be hypothesized to occur through the enantioselective development of chiral facets. As proposed by Sholl et al., chiral facets are high-index facets with Miller indices such that $h \neq k \neq l$ and $h \times k \times l \neq 0$, in an fcc lattice.[32] Such chiral facets, e.g., $(521)^S$ planes, can be theoretically seen as a combination of lower microfacets or terraces, and their handedness (*R*- or *S*-type facet) is decided by their arrangement (Figure S25, Supporting Information).[13] Moreover, chirality at the atomic level could help remove the mirror planes of the particle at the nanoscale. Since the {521}

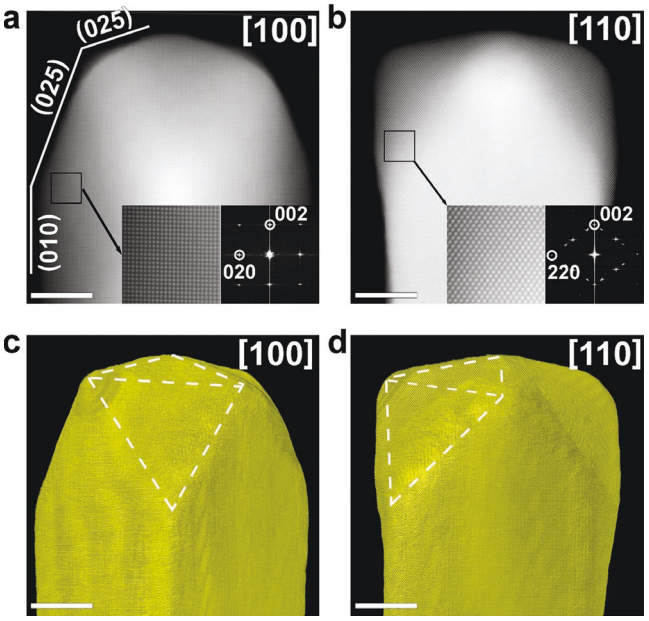

Figure 6. Atomic-resolution electron tomography characterization of an Au NR obtained after one chiral growth step. a,b) HAADF-STEM projections taken along [100] and [110] directions. Magnified regions showing atomic columns and corresponding Fourier transform patterns are presented as insets and indexed according to the Au fcc lattice. The white lines indicate the expected position of {010} and {520} types of facets (perpendicular to the projection plane). c,d) Visualization of the 3D reconstruction, taken along the indicated orientations. The white dashed lines indicate the position of {520} facets. All scale bars are 10 nm.

facets are quite close to the {520} facets (Figure S26, Supporting Information), here we use the chiral {521} facets as an example to illustrate how to achieve the symmetry descent from 4/mmm to 422. In the NR obtained after the first growth step, the four achiral {520} facets at the tips closer to the lateral sides can evolve into chiral {521} facets (Figure S27, Supporting Information). Each achiral facet would equally diverge into one *R* and one *S* facet if the growth is not enantioselective, thereby leading to achiral particles with a 4/mmm symmetry. However, if the process is enantioselective, the overexpression of *R* or *S* facets would help remove the mirror planes of the particle to obtain a 422 symmetry. This analysis could extend to any type of chiral facets, i.e., the enantioselective development from {520} facets into any type of chiral facets could realize the symmetry descent from 4/mmm to 422 symmetry. However, in real experiments the development of chiral facets might not be ideal, i.e., a perfectly well-defined chiral facet might not be formed during growth, and instead, ridges containing such chiral facet features might start to evolve from the tips. Nonetheless, the symmetry descent follows the same principle. If the expression of *R* and *S* facets is equal and non-enantioselective, particles with 4/mmm symmetry would be obtained (**Figure 7**; Figure S14, Supporting Information). The reason behind enantioselectivity appears thus to be related to the preferential binding of cys molecules, which may promote the growth of one of the enantiomeric facets, for example, $(521)^S$ versus $(52\text{–}1)^R$.

We thus employed density functional theory (DFT) simulations to investigate the role of cys in the symmetry descent of

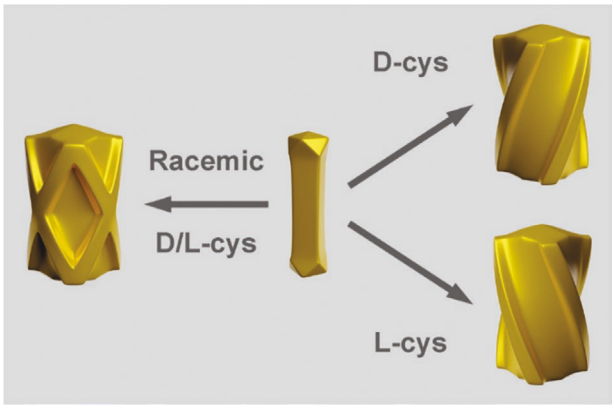

Figure 7. Schematic representation of enantioselective (using *D*- or *L*-cysteine) and non-enantioselective (using racemic *D*/*L*-cysteine) structural evolution of an Au NR after the first growth step.

Au NRs during seeded growth (see details in the Supporting Information: Computational Methods[33]). All relevant structures can be found in ioChem-BD.[34–37] We studied the configurational space of adsorbed *L*-cys on achiral low index facets and (520) facets, which are present in single-crystal Au NRs, as well as chiral $(521)^S$ and $(52–1)^R$ facets, as examples of *S*- and *R*-type surfaces, respectively. The adsorption energies (E_{ads}) for different *L*-cys conformations were computed. Figures S28–S30 (Supporting Information) show the results for the most stable adsorption conformations on each facet, both at low coverage (1 *L*-cys molecule per unit cell, corresponding to a surface coverage of 0.85–1.10 cys nm^{-2}, Table S2, Supporting Information) and at high coverage (2 or more *L*-cys molecules per unit cell, corresponding to a surface coverage of 1.72–2.97 cys nm^{-2}, Table S2, Supporting Information). Note that these surface concentrations are smaller than experimental estimates because the experimental value is an upper limit assuming all molecules being adsorbed on the metal surface, whereas an equilibrium between cys in solution and adsorbed on the surface would be a much more realistic scenario. At low coverage, E_{ads} was found to be more exothermic on chiral than on achiral facets, adsorption on an *S*-type surface being favored by 0.14 eV over that on an *R*-type surface. We then obtained the values of surface energies (γ_S) and *L*-cys adsorption-modified surface energies (γ'_S) (Figure S28b and Table S3, Supporting Information). The results show that chiral facets are energetically more stable than low-index facets and achiral (520) facets upon *L*-cys adsorption. This indicates that the surface evolution from low-index facets and achiral (520) facets into chiral facets is thermodynamically favorable. Furthermore, since the *L*-cys modified *S*-type surface has a lower energy than the *R*-type surface, we infer that *L*-cys is likely to assist more efficiently in the formation of *S*-type surfaces, thereby driving enantioselectivity. In the high coverage regime, adsorption on chiral facets is still favored over those on (520), (111), and (100) facets. However, the most exothermic E_{ads} and adsorption-modified surface energies were found to correspond to the (110) surface (Figure S28, Supporting Information). This result, together with the negligible difference in E_{ads} between *S*-type and *R*-type surfaces (0.02 eV), suggests that a high coverage of *L*-cys would hinder dissymmetric growth on Au NRs. This trend was also observed experimentally (Figure 5; Figure S12, Supporting Information), i.e., higher cys coverage leads to more intricate structures and lower optical activities.

To gain further insight on the shape evolution, equilibrium shapes were obtained through Wulff constructions,[38,39] based on the adsorption-modified surface energies (γ') (**Figure 8**; Table S3, Supporting Information) and the symmetry space group of the particle. First of all, the nanoparticle in Figure 6

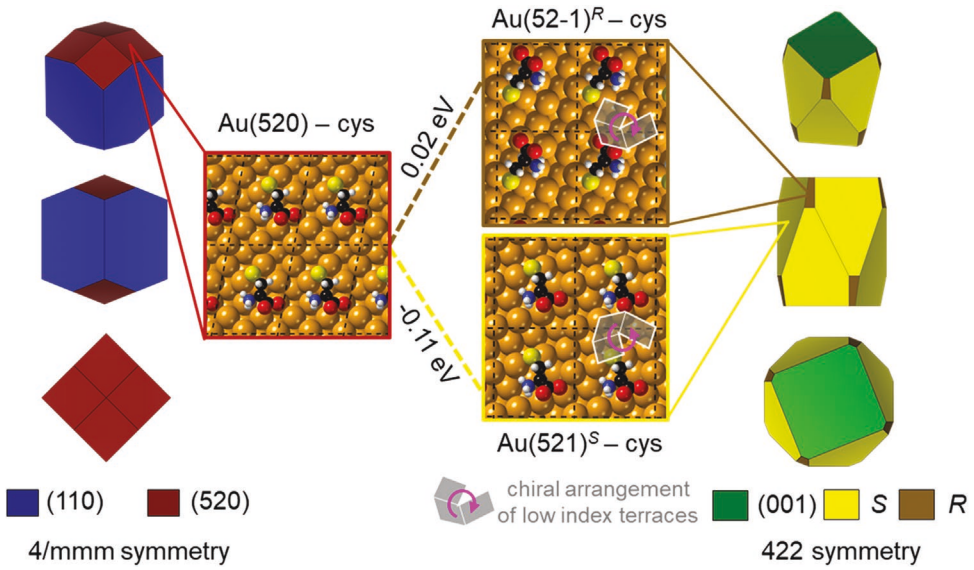

Figure 8. Left: oblique, side, and top view of a Wulff construction representing the shape of Au NRs after the first growth step. Center: reconstruction of a (520) surface at low coverage of *L*-cys, due to the difference of *L*-cys adsorption energies preferentially leading to a chiral $(521)^S$ facet over $(52–1)^R$. The dashed black frames denote the unit cells of the corresponding facets. Right: oblique, side, and top view of Wulff construction for a fourfold twisted Au NRs obtained by stabilizing $(521)^S$ facets over $(52–1)^R$.

(after the first growth step) can be described as surrounded by lateral {110} facets and {025} facets at the tips; from the available DFT data (adsorbate modified surface energies, Table S3, Supporting Information) this structure corresponds to the low coverage adsorption of cys, mainly on {520} facets. As determined from vacancy energy estimations, cys facilitates the mobility of kink atoms in {520} facets. In this manner, patterns similar to the kink features of the $(521)^S$ and $(52\text{–}1)^R$ could be obtained with low energies (<0.32 eV, Figures S31–S34, Supporting Information). The low energy demands for diffusion indicate that the cys-decorated surface is highly labile and the reconstruction process rendering the $(521)^S$ is exothermic by –0.11 eV, whereas that for $(52\text{–}1)^R$ is endothermic by 0.02 eV (Figure 8). The energy difference between *S*-type and *R*-type surfaces emerging from the adsorption of *L*-cys implies that objects obtained upon further growth will have an extra symmetry descent, removing all mirror planes. The structure obtained through chiral growth will thus present 422 symmetry (Figure S35, Supporting Information). The effect of chirality amplification on the shape of the nanoparticle can be observed from the ratio of the chiral surface energies ($\gamma_{(521)^S}/\gamma_{(52\text{–}1)^R}$, Figure S36, Supporting Information). Due to the mathematical nature of the Wulff construction, the final structure has an NR shape with fourfold planar caps that are 45° twisted though convex.[40] However, the lateral facets exhibit a similar morphology to that observed in the experiments (Figure 8; Figure S35, Supporting Information). Finally, if a high cys coverage is considered in the simulations, the energy difference between the surfaces is damped and the symmetry descent smooths out. Thus, the principal features behind cys-induced chiral growth on Au NRs can be interpreted with these thermodynamic models and the DFT energies.

3. Conclusion

Fourfold twisted Au NRs derive from cys-mediated multistep growth on single-crystal Au NRs. The obtained twisted NRs display *g*-factors up to –0.106. The NP morphologies and the optical activities can be finely tuned by varying cys concentration, growth temperature, and the size of the initial Au NRs. A detailed mechanistic study based on crystallographic analysis showed that the evolution of twisted facets may be the result of the development of chiral surfaces in the form of ridges through enantioselective surface evolutions. The proposed enantioselective growth is supported by DFT simulations of adsorption-modified surface energies. Altogether, this study provides fresh perspectives toward the large-scale preparation of chiral plasmonic NPs, but could also be extended to other compositions.

Supporting Information

Supporting Information is available from the Wiley Online Library or from the author.

Acknowledgements

This work was supported by the MCIN/AEI/10.13039/501100011033 (Grants PID2019-108954RB-I00, PID2020-117371RA-I00, PID2020-117779RB-I00, and Maria de Maeztu Units of Excellence Program from the Spanish State Research Agency Grant No. MDM-2017-0720), Xunta de Galicia/FEDER (Grant GRC ED431C 2020/09) and the European Regional Development Fund (ERDF). M.M., W.H., and S.B. acknowledge financial support from the European Commission under the Horizon 2020 Programme by ERC Consolidator grant no. 815128 (REALNANO). W.A. acknowledges financial support from the research program of AMOLF, which is partly financed by the Dutch Research Council (NWO). J.M.-V. and N.L. thank the Spanish Ministry of Science and Innovation for financial support (RTI2018-101394-B-I00, PID2021-122516OB-I00, and Severo Ochoa Grant MCIN/AEI/10.13039/501100011033 CEX2019-000925-S) and the Barcelona Supercomputing Center-MareNostrum (BSC-RES) for providing generous computer resources. S.G.-G. acknowledges the MCIN. B.N. acknowledges a postdoctoral fellowship of the Alexander von Humboldt Foundation. G.G.-R. acknowledges the Deutsche Forschungsgemeinschaft (GO 3526/1-1) for financial support. H.C. thanks Deutsche Forschungsgemeinschaft (DFG) SFB 1214 project B1 for funding. G.Z. acknowledges National Natural Science Foundation of China (Grant No. 21902148).

Open access funding enabled and organized by Projekt DEAL.

Conflict of Interest

The authors declare no conflict of interest.

Data Availability Statement

The data that support the findings of this study are available from the corresponding author upon reasonable request.

Keywords

Au nanorods, chiral seeded growth, plasmonic optical activity, twisted nanoparticles, Wulff construction

Received: September 9, 2022
Revised: October 3, 2022
Published online: November 17, 2022

[1] L. A. Nguyen, H. He, C. Pham-Huy, *Int J Biomed Sci* **2006**, *2*, 85.
[2] A. Visheratina, N. A. Kotov, *CCS Chem.* **2020**, *2*, 583.
[3] B. Ni, H. Cölfen, *SmartMat* **2021**, *2*, 17.
[4] A. Ben-Moshe, B. M. Maoz, A. O. Govorov, G. Markovich, *Chem. Soc. Rev.* **2013**, *42*, 7028.
[5] T.-T. Zhuang, Y. Li, X. Gao, M. Wei, F. P. García de Arquer, P. Todorović, J. Tian, G. Li, C. Zhang, X. Li, L. Dong, Y. Song, Y. Lu, X. Yang, L. Zhang, F. Fan, S. O. Kelley, S.-H. Yu, Z. Tang, E. H. Sargent, *Nat. Nanotechnol.* **2020**, *15*, 192.
[6] R. Naaman, D. H. Waldeck, *J. Phys. Chem. Lett.* **2012**, *3*, 2178.
[7] S. Alwan, Y. Dubi, *J. Am. Chem. Soc.* **2021**, *143*, 14235.
[8] L. Xu, X. Wang, W. Wang, M. Sun, W. J. Choi, J.-Y. Kim, C. Hao, S. Li, A. Qu, M. Lu, X. Wu, F. M. Colombari, W. R. Gomes, A. L. Blanco, A. F. de Moura, X. Guo, H. Kuang, N. A. Kotov, C. Xu, *Nature* **2022**, *601*, 366.
[9] B. List, R. A. Lerner, C. F. Barbas, *J. Am. Chem. Soc.* **2000**, *122*, 2395.
[10] K. A. Ahrendt, C. J. Borths, D. W. C. MacMillan, *J. Am. Chem. Soc.* **2000**, *122*, 4243.
[11] S. Che, Z. Liu, T. Ohsuna, K. Sakamoto, O. Terasaki, T. Tatsumi, *Nature* **2004**, *429*, 281.

[12] K. Robbie, G. Beydaghyan, T. Brown, C. Dean, J. Adams, C. Buzea, *Rev. Sci. Instrum.* **2004**, *75*, 1089.
[13] N. Shukla, A. J. Gellman, *Nat. Mater.* **2020**, *19*, 939.
[14] J. Fan, N. A. Kotov, *Adv. Mater.* **2020**, *32*, 1906738.
[15] H.-E. Lee, H.-Y. Ahn, J. Mun, Y. Y. Lee, M. Kim, N. H. Cho, K. Chang, W. S. Kim, J. Rho, K. T. Nam, *Nature* **2018**, *556*, 360.
[16] G. González-Rubio, J. Mosquera, V. Kumar, A. Pedrazo-Tardajos, P. Llombart, M. Solís Diego, I. Lobato, G. Noya Eva, A. Guerrero-Martínez, M. Taboada José, F. Obelleiro, G. MacDowell Luis, S. Bals, M. Liz-Marzán Luis, *Science* **2020**, *368*, 1472.
[17] S. Wang, L. Zheng, W. Chen, L. Ji, L. Zhang, W. Lu, Z. Fang, F. Guo, L. Qi, M. Liu, *CCS Chem.* **2020**, *3*, 2473.
[18] E. C. Dreaden, A. M. Alkilany, X. Huang, C. J. Murphy, M. A. El-Sayed, *Chem. Soc. Rev.* **2012**, *41*, 2740.
[19] N. Li, P. Zhao, D. Astruc, *Angew. Chem., Int. Ed.* **2014**, *53*, 1756.
[20] J. Kumar, H. Eraña, E. López-Martínez, N. Claes, V. F. Martín, D. M. Solís, S. Bals, A. L. Cortajarena, J. Castilla, L. M. Liz-Marzán, *Proc. Natl. Acad. Sci. USA* **2018**, *115*, 3225.
[21] K. Hou, J. Zhao, H. Wang, B. Li, K. Li, X. Shi, K. Wan, J. Ai, J. Lv, D. Wang, Q. Huang, H. Wang, Q. Cao, S. Liu, Z. Tang, *Nat. Commun.* **2020**, *11*, 4790.
[22] G. Zheng, J. He, V. Kumar, S. Wang, I. Pastoriza-Santos, J. Pérez-Juste, L. M. Liz-Marzán, K.-Y. Wong, *Chem. Soc. Rev.* **2021**, *50*, 3738.
[23] H.-Y. Ahn, S. Yoo, N. H. Cho, R. M. Kim, H. Kim, J.-H. Huh, S. Lee, K. T. Nam, *Acc. Chem. Res.* **2019**, *52*, 2768.
[24] B. Goris, S. Bals, W. Van den Broek, E. Carbó-Argibay, S. Gómez-Graña, L. M. Liz-Marzán, G. Van Tendeloo, *Nat. Mater.* **2012**, *11*, 930.
[25] M. J. Walsh, W. Tong, H. Katz-Boon, P. Mulvaney, J. Etheridge, A. M. Funston, *Acc. Chem. Res.* **2017**, *50*, 2925.
[26] G. González-Rubio, V. Kumar, P. Llombart, P. Díaz-Núñez, E. Bladt, T. Altantzis, S. Bals, O. Peña-Rodríguez, E. G. Noya, L. G. MacDowell, A. Guerrero-Martínez, L. M. Liz-Marzán, *ACS Nano* **2019**, *13*, 4424.
[27] M. Grzelczak, A. Sánchez-Iglesias, B. Rodríguez-González, R. Alvarez-Puebla, J. Pérez-Juste, L. M. Liz-Marzán, *Adv. Funct. Mater.* **2008**, *18*, 3780.
[28] W. Heyvaert, A. Pedrazo-Tardajos, A. Kadu, N. Claes, G. González-Rubio, L. M. Liz-Marzán, W. Albrecht, S. Bals, *ACS Mater. Lett.* **2022**, *4*, 642.
[29] V. Myroshnychenko, J. Rodríguez-Fernández, I. Pastoriza-Santos, A. M. Funston, C. Novo, P. Mulvaney, L. M. Liz-Marzán, F. J. García de Abajo, *Chem. Soc. Rev.* **2008**, *37*, 1792.
[30] D. M. Solís, J. M. Taboada, F. Obelleiro, L. M. Liz-Marzán, F. J. García de Abajo, *ACS Nano* **2014**, *8*, 7559.
[31] L. Scarabelli, A. Sánchez-Iglesias, J. Pérez-Juste, L. M. Liz-Marzán, *J. Phys. Chem. Lett.* **2015**, *6*, 4270.
[32] D. S. Sholl, A. Asthagiri, T. D. Power, *J. Phys. Chem. B* **2001**, *105*, 4771.
[33] J. Morales-Vidal, N. López, M. A. Ortuño, *J. Phys. Chem. C* **2019**, *123*, 13758.
[34] M. Álvarez-Moreno, C. de Graaf, N. López, F. Maseras, J. M. Poblet, C. Bo, *J. Chem. Inf. Model.* **2015**, *55*, 95.
[35] J. Morales-Vidal, Database. https://doi.org/10.19061/iochem-bd-1-114.
[36] J. Morales-Vidal, Database. https://doi.org/10.19061/iochem-bd-1-252.
[37] C. Bo, F. Maseras, N. López, *Nat. Catal.* **2018**, *1*, 809.
[38] G. Wulff, *Z. Kristallogr. Cryst. Mater.* **1901**, *34*, 449.
[39] G. D. Barmparis, Z. Lodziana, N. Lopez, I. N. Remediakis, *Beilstein J. Nanotechnol.* **2015**, *6*, 361.
[40] Q. Li, M. Rellán-Piñeiro, N. Almora-Barrios, M. Garcia-Ratés, I. N. Remediakis, N. López, *Nanoscale* **2017**, *9*, 13089.